CHEMISTRY OF MATERIALS

pubs.acs.org/cm

Article

Spatiotemporal Route to Understanding Metal Halide Perovskitoid Crystallization

Mansoor Ani Najeeb Nellikkal, Rodolfo Keesey, Margaret Zeile, Venkateswaran Shekar, Zhi Li, Nicholas Leiby, Matthias Zeller, Emory M. Chan, Joshua Schrier, and Alexander J. Norquist*

Cite This: https://doi.org/10.1021/acs.chemmater.2c00247

Read Online

ACCESS | Metrics & More | Article Recommendations | Supporting Information

ABSTRACT: A spatiotemporal experimental route is reported for the antisolvent vapor diffusion crystal growth of metal halide perovskitoids. A computational analysis combining automated image capture and diffusion modeling enables the determination of the critical concentrations required for nucleation and crystal growth from a single experiment. Five different solvent systems and ten distinct organic ammonium iodide salts were investigated with lead iodide, from which nine previously unreported compounds were discovered. Automated image capture of the mother liquor and antisolvent vials was used to determine changes in solution meniscus positions and detect the nucleation event location. Matching the observations to a numerical solution of Fick's second law diffusion model enables the calculation of reactant, solvent, and antisolvent concentrations at both the time and position of the first stable nucleation and crystal growth. A machine learning model was trained on the resulting data, and it reveals solvent- and amine-specific crystallization tendencies. Solvent systems that interact more weakly with dissolved lead species promote crystallization, while those with stronger interactions can prevent crystallization through increased solubilities. Organic amines that interact more strongly with inorganic components and exhibit greater rigidity are more likely to be incorporated into crystalline products.

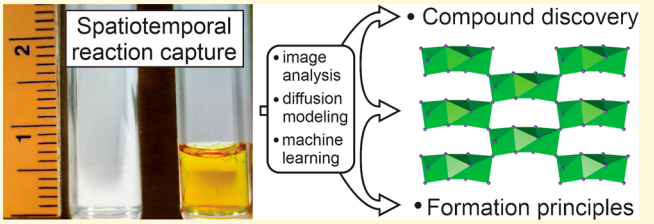

INTRODUCTION

Metal halide perovskitoids, the subject of intense interest owing to their promise in solar cell applications,[1−5] photodetection,[6−9] and lasers,[10−12] can be created in different forms using a range of synthetic techniques. Single crystalline samples are grown using a range of solution phase methods,[13−17] with antisolvent vapor-assisted crystallization (ASVC) being used commonly because of the high quality samples that are produced and the lack of temperature management challenges present in inverse temperature crystallization methods.[18−21] In AVSC, the slow diffusion of the antisolvent (AS) into the perovskitoid precursor solution reduces the solubility of the target compounds and induces precipitation. A range of experimental parameters affect an ASVC experiment, including the nature of the solvent and AS, organic cation structure, and relative reactant concentrations. The conditions required for nucleation and crystal growth directly affect the properties of the resulting crystalline products.[22] As such, the elucidation of these critical reaction parameters is paramount in understanding this chemistry. However, the critical factors leading to nucleation remain unresolved, despite the number of studies investigating ASVC perovskitoid crystallization.

A central challenge with ASVC perovskitoid crystallization lies in the large experimental space, owing to the interplay between reactant, solvent, and antisolvent concentrations, each of which vary during the course of an experiment. High-throughput techniques have been applied to explore these possible combinations by setting up many possible reactions. Kirman *et al.* described the use of a protein drop setter to perform antisolvent vapor diffusion experiments to explore ASVC growth of phenethylammonium lead bromide and 3-picolylammonium lead chloride perovskitoids.[23] Although their system could image reaction compositions over time, imaging the reaction system from above only allows for observing whether a given mother liquor and antisolvent composition gives rise to crystal formation. Similarly, Li *et al.* described a liquid handling robot-based system for performing high-throughput ASVC experiments to explore mother liquor and antisolvent composition variables; likewise, only the final composition is reported,[24] obscuring the critical parameter required to induce crystallization. In contrast, here, we report a unique spatiotemporal approach that replaces a parallel set of experiments in space (i.e., conducted in separate spatial vials and with separate materials) with a smaller set of experiments conducted over time. Our approach enables the determination

Received: January 25, 2022
Revised: May 26, 2022

of both the time and position of nucleation and crystal growth, by imaging a single reaction orthogonal to the direction of diffusion propagation. Fitting these observations to a numerical antisolvent diffusion model provides the critical concentrations of each reactant required for crystal growth (Figure 1). In this

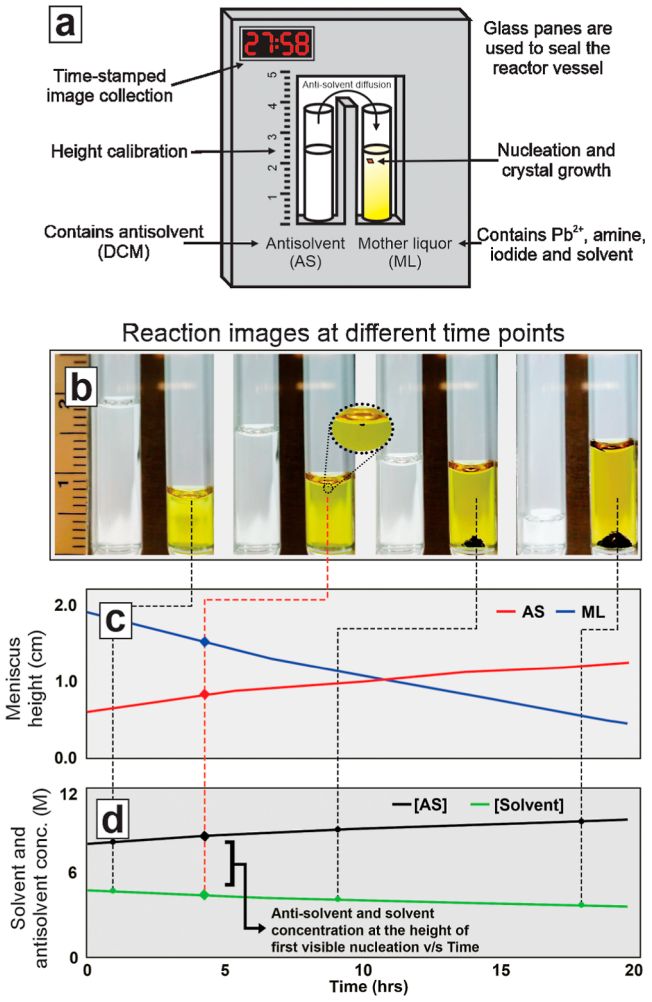

Figure 1. Spatiotemporal reaction design, including the (a) reaction block diagram, (b) reaction image capture, (c) mother liquor (ML), and antisolvent (AS) meniscus positions, and nucleation detection and (d) calculated solvent and antisolvent concentrations as a function of time.

way, observing the progress of a single experiment in time can be used to scan over a wide range of reactant, solvent, and antisolvent concentrations. A set of individual reactions was conducted using PbI_2, ten different organic ammonium iodide salts, and five solvent systems in order to better understand the generalized requirements for such syntheses. The spatiotemporal reaction design allows for the elucidation of these critical reaction parameters from a single experiment in each reagent combination. The critical concentration parameters along with the computed chemical descriptors of the reaction components were pooled into a rich data set and used for machine learning analysis in the form of an explanatory decision tree model to uncover complex trends observed in the data.

EXPERIMENTAL SECTION

Materials. All reagents were purchased from commercial sources and used without further purification. Lead(II) iodide (99%), formic acid (FA, ≥95%), γ-butyrolactone (GBL, ≥99%), dimethyl sulfoxide (DMSO, ≥99.9%), dimethylformamide (DMF, 99.8%), and dichloromethane (DCM, ≥99.8%) were purchased from Sigma-Aldrich. Ten organic ammonium iodide salts were purchased from GreatCell Solar: methylammonium iodide (ma, 99.99%), ethylammonium iodide (ea, >99.8%), 1,3-dimethylammonium iodide (1,3-dap, >99.8%), acetamidinium iodide (acet, >99%), *N*,*N*-dimethylammonium iodide (dmed, >99.8%), *N*,*N*-diethyl-1,3-diaminopropane iodide (dedap, >99.8%), cyclohexylmethylammonium iodide (chma, >99.8%), 1-(2-aminoethyl)pyrrolidinium iodide (aep, >99.8%), 1,4-benzene diammonium iodide (dabz, >99.8%), and phenethylammonium iodide (phenea, >99%).

Spatiotemporal Reaction Design. All reactions were conducted using an antisolvent vapor diffusion crystallization technique. Reagent solutions (180 μL), FAH (20 μL), and the antisolvent (800 μL, DCM) were placed in separate 1 mL cylindrical glass vials. These clear vials were placed in an aluminum block and sealed using glass panes to prevent escape of vapors, shown in Figure 1a. The reactions were allowed to proceed for 24 h at room temperature. Although the temperatures of the reactions were not actively controlled, passive measurements were made during the course of the experiments. The average laboratory temperature was 25.5 °C. Temperature fluctuations during the course of each recorded experiment were observed, with an average standard deviation of 0.59 °C. Plots of representative temperature fluctuations are provided in Supporting Information, Figure S2. Optical images of the reaction blocks were captured every 60 s for each crystallization experiment using a microscope camera. At the end of the reaction, the contents of the vials were scored using the four-point scale, no solids, fine powder, and small or large crystallites, as described in more detail in the Supporting Information, consistent with previous work.[25] After reaction, the reactor block was opened in air, and the solid products were recovered by vacuum filtration. Powder X-ray diffraction data were collected on all solid reaction products. Ten different organic ammonium iodide salts, shown in Figure 2, and five

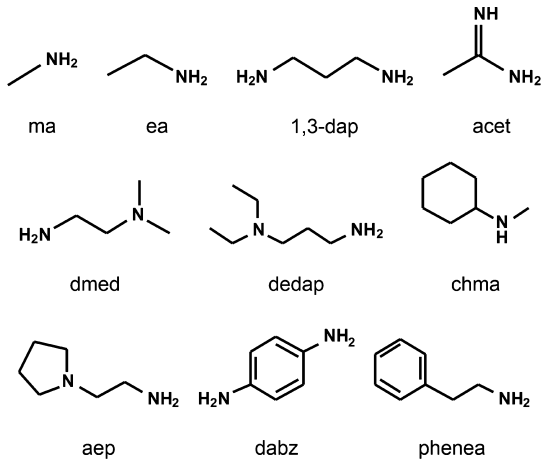

Figure 2. Ten organic amines used in this study.

solvent systems were selected for study. These solvent systems included GBL, GBL/DMF, DMF, DMF/DMSO, and DMSO. Reaction outcomes are shown in Figure 3. Nine new compounds (**1**–**9**) were observed, in addition to seven previously reported phases (**A**–**G**), as listed in Table 1.

Targeted bench-scale crystal growth experiments were performed to generate single crystals for structural characterization, using a reactor design shown in Figure S26. PbI_2/ammonium iodide stock solutions in the respective solvent (GBL, GBL/DMF, DMF, DMF/DMSO, or DMSO) were prepared at 75 °C and stirred at 450 rpm for 1 h. Aliquots (200 μL) of mother liquor solutions were transferred to 1 mL clear shell vials to which 20 μL of FAH was added. These solutions were mixed on a heater shaker for 20 min. After cooling to room temperature, the reaction vials were placed inside 20 mL scintillation vials containing

https://doi.org/10.1021/acs.chemmater.2c00247
Chem. Mater. XXXX, XXX, XXX−XXX

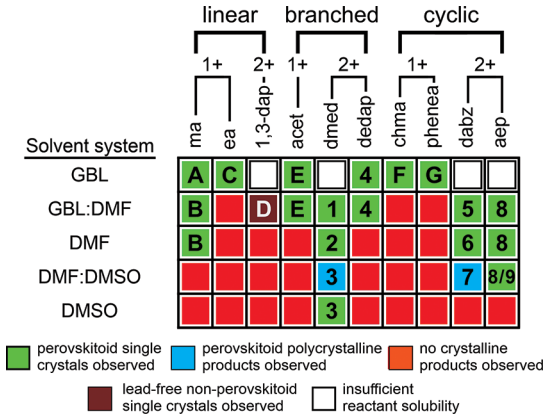

Figure 3. Reaction outcomes as a function of organic amine and solvent system.

approximately 1.5 mL of DCM and sealed with a PTFE-lined solid-top storage cap. Reactions were allowed to run for at least 24 h. The calculated powder diffraction patterns were compared to the experimental diffraction data from the spatiotemporal experiments to ensure that bench-scale products were identical to the initially identified products. Specific reaction details for the mixtures that gave rise to compounds **1**−**9** are available in the Supporting Information.

Image Processing. A Python interface was used for the manual annotation of key parts of the reaction images. Side-on views of the mother liquor and antisolvent reaction vials were collected. A ruler was attached to the reaction block to calibrate image pixels to physical distance measurements. Users were shown evenly spaced images across each reaction's time lapse image set. Meniscus positions for both the mother liquor and antisolvent were user-annotated. Additionally, the script was used to identify when and where nucleation first occurred by showing the time lapse images to the user following a binary search pattern. The difference between the meniscus position and the bottom of the test tube determines the height of the solution at each time. These solution height measurements were used to calculate the diffusion rate of the antisolvent. The corners of each crystal were denoted manually, allowing for the calculation of the mean crystal pixel position at the point to crystal formation. This Python code via GitHub is detailed in the Supporting Information section.

Powder X-ray Diffraction. Powder X-ray diffraction measurements were performed on a Rigaku MiniFlex X-ray diffractometer using CuKα radiation (1.5418 Å). Powder X-ray diffraction scans were collected on all reaction products, and these plots are provided in the Supporting Information (S5−S25).

Single-Crystal X-Ray Diffraction. Data were collected using a Bruker Quest CMOS diffractometer with a fixed chi angle, a sealed tube fine focus X-ray tube (Mo Kα radiation, λ = 0.71073 Å), a single-crystal curved graphite incident beam monochromator, a photon II area detector, and an Oxford Cryosystems low-temperature device. A single crystal was mounted on a MiTeGen micromesh mount using a trace of Fomblin oil and cooled *in situ* to 150(2) K for data collection. Frames were collected, reflections were indexed and processed, and the files were scaled and corrected for absorption using APEX3, SAINT, and SADABS or TWINABS. For compounds **1**, **2**, and **4**−**9**, the heavy atom positions were determined using SIR92. All other nonhydrogen sites were located from Fourier difference maps. All nonhydrogen sites were refined using anisotropic thermal parameters using full matrix least-squares procedures on F_o^2 with $I > 3\int(I)$. Hydrogen atoms were placed in geometrically idealized positions. Calculations for compounds **1**, **2**, and **4**−**9** were performed using Crystals v.14.23c. The structure of compound **3** was found to be nonmerohedrally twinned by a 180° rotation around the real *a*-axis. The structure was solved by direct methods using ShelXS from only the nonoverlapping reflections of component 1. The structure was refined using Shelxl with the hklf 5 routine with all reflections of component 1 (including the overlapping ones), resulting in a BASF value of 0.5490(8). Additional details are given in the .cif for compound **3**. Relevant crystallographic data for compounds **1**−**9** are listed in Table 2.

Antisolvent Diffusion Modeling. An antisolvent diffusion model was created to elucidate the critical concentrations for nucleation and crystallization. The concentration profile of the mother liquor was calculated using a finite volume approximation of Fick's second law to simulate one-dimensional liquid diffusion.[26] The differential equation was integrated numerically by discretizing the experimental solution into bins, where each bin has a defined height and starting concentration for each species, see Figure 4a. Diffusion from bin to bin was calculated based on the distances from the centers of each bin. The height of each bin is directly related to the concentration of the species occupying it. As the species diffuse into and out of each bin, the height of the bin changes and the distance for diffusion subsequently changes. Fixed boundaries are not used because the total volume of the solution increases during the course of the experiment. The top bin has an ingress of the antisolvent from the gaseous phase and evaporation of the antisolvent species from the solution. These two parameters vary between experiments and are optimized to fit the experimental height as a function of time. With a satisfactory fit, the model reasonably reflects the experimental data. The simulation is stopped at the first appearance of a crystal, allowing us to neglect any mass transport from gravitational settling of the crystal.

The diffusion simulation requires the experimentally determined diffusion coefficient for the antisolvent through each solution. This is

Table 1. Reaction Products

compound	formula	inorganic dimensionality	reference
A	$[ma][PbI_3]$	3D	52
B	$[ma][Pb_3I_8]\cdot 2DMF$	1D	53
C	$[ea][PbI_3]$	1D	54
D	$[dapH_2][I]_2$		55
E	$[acetH][PbI_3]$	1D	25
F	$[chmaH]_2[PbI_4]$	2D	25
G	$[pheneaH]_2[PbI_4]$	2D	56
1	$[dmedH_2]_3[Pb_2I_9][CO_2H]$	0D	this work
2	$[dmedH_2]_3[Pb_3I_{12}]\cdot 4DMF$	0D	this work
3	$[dmedH_2]_2[Pb_3I_{10}]\cdot 2DMSO$	1D	this work
4	$[dedapH]_2[PbI_6]$	0D	this work
5	$[dabzH_2][PbI_3]_2\cdot 2GBL\cdot 2DMF$	1D	this work
6	$[dabzH_2][PbI_3]_2\cdot 4DMF$	1D	this work
7	$[dabzH_2][PbI_3]_2\cdot 4DMSO$	1D	this work
8	$[aepH_2]_2[Pb_3I_{10}]\cdot 2DMF$	2D	this work
9	$[aepH_2]_4[Pb_3I_{12}][CO_2H]_2\cdot 2DMSO$	0D	this work

https://doi.org/10.1021/acs.chemmater.2c00247
Chem. Mater. XXXX, XXX, XXX−XXX

Table 2. Crystallographic Data for Compounds 1−9

compound	$[C_4H_{14}N_2]_3[Pb_2I_9]$ $[CO_2H]$ (**1**)	$[C_4H_{14}N_2]_3[Pb_3I_{12}]\cdot 4C_3H_7NO$ (**2**)	$[C_4H_{14}N_2]_2[Pb_3I_{10}]\cdot 2C_2H_6SO$ (**3**)	$[C_7H_{20}N_2]_2[PbI_6]$ (**4**)	$[C_6H_{10}N_2][PbI_3]_2\cdot 2C_4H_6O_2\cdot 2C_3H_7NO$ (**5**)
formula	$C_{13}H_{43}I_9N_6O_2Pb_2$	C_{24} $H_{70}I_{12}N_{10}O_4Pb_3$	$C_{12}H_{40}I_{10}N_4O_2Pb_3S_2$	$C_{14}H_{40}I_6N_4Pb_1$	$C_{20}H_{36}I_6N_4O_6Pb_2$
fw	1872.06	2707.35	2227.17	1233.12	1604.36
space group	$P\bar{1}$ (no. 2)	$P\bar{1}$ (no. 2)	$P2_1/n$ (no. 14)	$P2_1/n$ (no. 14)	$P\bar{1}$ (no. 2)
a (Å)	9.34390 (5)	8.9706 (4)	10.4168 (7)	11.39480 (7)	8.0944 (4)
b (Å)	9.85820 (6)	18.4476 (8)	11.7679 (6)	11.50440 (7)	10.6456 (6)
c (Å)	22.71670 (13)	19.9034 (9)	18.5962 (11)	11.92840 (7)	12.8019 (7)
α (deg)	93.1160 (2)	76.935 (2)	90.0	90.0	112.991 (2)
β (deg)	90.2040 (2)	87.338 (2)	96.848 (3)	102.0140 (2)	98.921 (2)
γ (deg)	105.1086 (19)	85.969 (2)	90.0	90.0	95.953 (2)
V (Å^3)	2016.9 (2)	3199.0 (2)	2263.3 (2)	1529.45 (16)	986.72 (9)
Z	2	2	2	2	2
ρ_{calc} (g cm^{-3})	3.082	2.811	3.268	3.082	2.700
λ (Å)	0.71073	0.71073	0.71073	0.71073	0.71073
T (K)	150 (2)	150 (2)	150 (2)	150 (2)	150 (2)
μ (mm^{-1})	15.244	13.699	18.059	11.579	13.246
R_1	0.0425	0.0342	0.0486	0.0201	0.0289
wR_2	0.0867	0.0494	0.1040	0.0404	0.0503

compound	$[C_6H_{10}N_2][PbI_3]_2\cdot 4C_3H_7NO$ (**6**)	$[C_6H_{10}N_2][PbI_3]_2\cdot 4C_2H_6SO$ (**7**)	$[C_6H_{16}N_2]_2[Pb_3I_{10}]\cdot 2C_3H_7NO$ (**8**)	$[C_6H_{16}N_2]_4[Pb_3I_{12}]\cdot 2CHO_2\cdot 2SOC_2H_6$ (**9**)
formula	$C_{18}H_{38}I_6N_6O_4Pb_2$	$C_{14}H_{34}I_6N_2O_4Pb_2S_4$	$C_{18}H_{46}I_{10}N_6O_2Pb_3$	$C_{30}H_{78}I_{12}N_8O_6Pb_3S_2.00$
fw	1578.36	1598.53	2269.25	2855.60
space group	$P2_1/c$ (no. 14)	$P2_1/c$ (no. 14)	$C2/c$ (no. 15)	$P\bar{1}$ (no. 2)
a (Å)	9.7427 (6)	9.1442 (3)	23.77360 (15)	10.0789 (6)
b (Å)	24.7644 (16)	24.0936 (8)	9.45230 (6)	18.4456 (13)
c (Å)	7.9702 (5)	8.2387 (3)	21.04520 (12)	19.7271 (13)
α (deg)	90.0	90.0	90.0	74.235(3)
β (deg)	95.493(3)	94.6821(13)	90.3600(2)	77.155(2)
γ (deg)	90	90.0	90.0	82.993(2)
V (Å^3)	1914.2 (2)	1809.07 (11)	4729.1 (5)	3433.8 (4)
Z	2	2	4	2
ρ_{calc} (g cm^{-3})	2.738	2.934	3.187	2.762
λ (Å)	0.71073	0.71073	0.71073	0.71073
T (K)	150 (2)	150 (2)	150 (2)	150 (2)
μ (mm^{-1})	13.652	14.666	17.206	12.830
R_1	0.0429	0.0232	0.0363	0.0482
wR_2	0.1122	0.0440	0.0912	0.0467

https://doi.org/10.1021/acs.chemmater.2c00247
Chem. Mater. XXXX, XXX, XXX−XXX

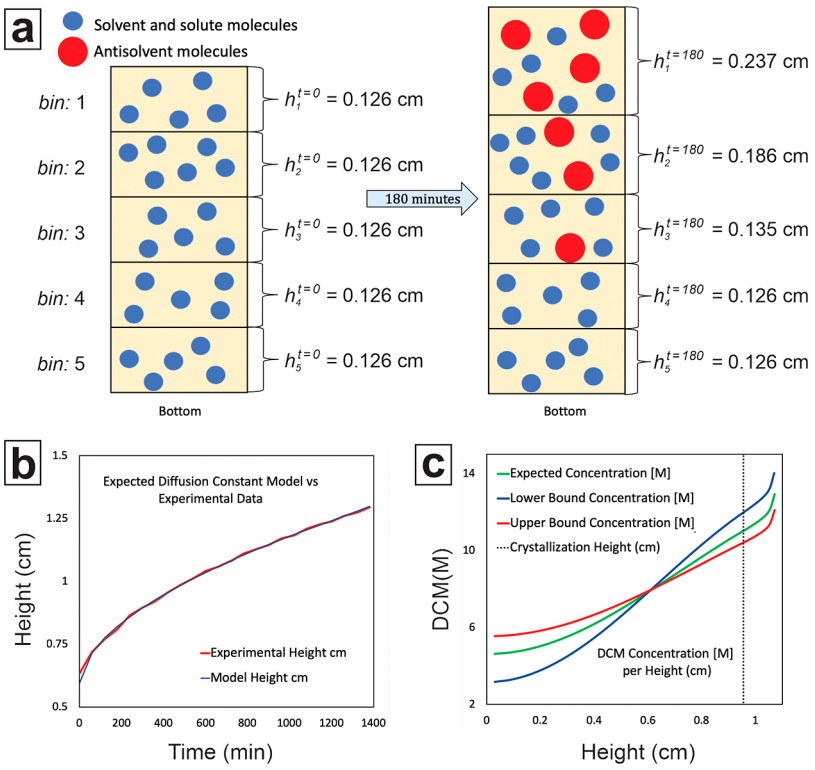

Figure 4. Diffusion modeling, including a (a) diagram indicating how the influx of antisolvent molecules affect bin heights and (b) model height fits and (c) concentration profile at crystallization in the PbI_2/aep/DMF/DMSO system.

Table 3. Calculated DCM Diffusion Coefficients

solvent	refractive index	expected diffusion coefficient (D, m^2/s)	lower bound diffusion coefficient (D, m^2/s)	upper bound diffusion coefficient (D, m^2/s)	propagated uncertainty range (plus or minus) (D, m^2/s)
GBL	1.4348	5.26×10^{-10}	7.00×10^{-11}	9.82×10^{-10}	4.56×10^{-10}
GBL/DMF	1.4783	1.08×10^{-10}	4.00×10^{-12}	2.12×10^{-10}	1.04×10^{-10}
DMF	1.42075	5.55×10^{-10}	0.00	1.14×10^{-9}	5.66×10^{-10}
DMF/DMSO	1.436	2.07×10^{-10}	1.32×10^{-10}	2.82×10^{-10}	7.50×10^{-11}
DMSO	1.4305	1.24×10^{-9}	9.61×10^{-10}	1.52×10^{-9}	2.79×10^{-10}

obtained using a laser diffraction experiment, which measures the diffusion rate for each experimental condition by observing changes in the refractive index of the mixture,[27,28] see the Supporting Information. Note that only the diffusion of the antisolvent in each solvent was determined owing to the experimental challenges of performing the laser refraction measurements in the presence of solutes. However, at the relatively low (0.5 M) electrolyte concentrations, the diffusion constant should not vary by more than ±5%,[29] minimizing the errors introduced through exclusion of solutes. However, these experiments rely on the image detection of height for a diffracted beam. This method is subject to the measurement error, and the diffusion coefficients were found to deviate by an order of magnitude between neat solvent systems and mixtures of the same chemicals. To account for this uncertainty in the model, the possible error in laser diffraction measurement was propagated through the calculation of the diffusion coefficient. This results in three values, the diffusion coefficient with the lowest uncertainty and its associated upper bound and lower bound. Measured refractive indices for each solvent system, along with calculated diffusion coefficient parameters, are listed in Table 3.

The rates of evaporation and condensation of the antisolvent are free parameters. For each experiment, they are optimized to fit the model height growth to the experimental data, see Figure 4b. The best fitting evaporation and condensation rates are calculated using the Nelder–Mead algorithm,[30] with the sum square difference between the model and experimental height growth as the objective function. These optimizations are run three times for each experiment to determine the optimal parameters under the expected diffusion coefficient, the lower bound, and the upper bound, see Figure 4b.

After determining the condensation and evaporation rates, the model is fully constrained, allowing us to compute the solute (both inorganic and organic) and antisolvent compositions at each height and time. Calculated values of the antisolvent, solvent, FAH, and solutes (both inorganic and organic) for which crystallization was observed are provided in the Supporting Information in Table S14. However, as the model assumes a constant condensation rate of the antisolvent into the solution, the simulation must be stopped before the antisolvent supply runs out. As the antisolvent build-up rate differs for every experiment and crystallization occurs at various times, a cutoff was implemented based upon solution buildup rather than the elapsed time. The cutoff in the solution height was set to 0.72 cm. This stopped all models before the antisolvent supply ran out. After determining this cutoff, the model can then be used to calculate the concentration profile of the solution at the time and location of crystallization. The model returns the expected concentration of each species, as well as the upper and lower bound, see Figure 4c. A more detailed description of the diffusion modeling work is present in the Supporting Information, and the MATLAB R2020b source code used to perform the simulations is available via Github, as detailed in the Supporting Information section.

Software. ESCALATE,[31] a custom-developed software pipeline, was used to specify experimental and stock solution preparation parameters, provide instructions for human operators, and capture experiment results and observations. The algorithms for data

https://doi.org/10.1021/acs.chemmater.2c00247
Chem. Mater. XXXX, XXX, XXX−XXX

visualization and analysis were written in Python 3.6 in Jupyter notebooks using the following libraries: Numpy 1.14.6, Pandas 0.22.0, Scipy 1.0.1, Matplotlib 3.1.0, and Scikit-learn 0.19.2.

Machine Learning. Weka was used to generate a J48 decision tree, which is a Java implementation of the C4.5 decision tree algorithm.[32−34] The algorithm is provided with the full set of descriptors (provided in the Supporting Information) and selects the descriptors that produce the "best" split of the data using multiway, predictive model split, and entropy criteria.[35] An unpruned tree with a confidence factor of 0.25 was used, and the minimum number of samples per leaf node was set to 2. The set number of folds for reduced error pruning was 3, and a seed value of 1 was used. A total of 56 features were used to describe the ASVC perovskitoid synthesis reactions. These features include 44 organoammonium descriptors, 3 solvent details, and 9 descriptors derived from the diffusion model. Input data sets and Weka input files used to perform these calculations are available via GitHub, as detailed in the Supporting Information section.

RESULTS AND DISCUSSION

The versatility of ASVD crystallization lies in the technique's ability to slowly alter the mother liquor properties until nucleation and crystallization occur. While the compounds that can be synthesized using this technique can differ from other crystal growth routes, such as inverse temperature crystallization, ASVD crystallization operates as an important route for materials discovery, as seen in the new compounds reported here. This dynamic process, in which the antisolvent slowly diffuses into the mother liquor, allows one to scan a range of crystallization conditions with properties between the pure solvent and (nearly) pure antisolvent. As the antisolvent generally diffuses into the mother liquor slowly, solution properties change gradually, promoting large high-quality single crystals. However, if one wishes to understand the role of any specific reactant in such a crystallization or wishes to probe the trends across reactant sets, observing whether or not a reaction results in crystallization is insufficient. Instead, the critical concentrations that allow for nucleation and crystallization of each species must be elucidated. Unfortunately, the apparent simplicity of the AVSD technique hides the true complexity at play.

The synthetic approach described here is intentionally designed to enable the determination of the critical reactant concentrations for each system in a single experiment. The diffusion of the antisolvent through the mother liquor creates an antisolvent (and solvent) concentration gradient and increases the total volume of the solution. As such, a wide range of reactant, solvent, and antisolvent concentrations are created as functions of both time and position. By capturing time-dependent images of each reaction from the side of each vial (i.e., orthogonal to the direction of mass transport), we are able to determine both when and where nucleation and crystal growth occur. A numerical antisolvent diffusion model can convert the observed nucleation time and position to the critical species concentrations, see Figure 1. The power of this approach lies in the ability to determine the conditions required for crystallization in a single experiment. Parallel experiments in each system are not required, resulting in a much more efficient process.

A custom reactor block (Figure 1a) was used to acquire images of the reaction vials every 60 s over the course of 24 h. Time-stamped images were collected and analyzed with a custom script to determine meniscus positions, as well as the times and positions of nucleation and crystal growth. Ten different organic amines, shown in Figure 2, and five different solvent systems were explored. Of the 50 potential experiments, 46 were conducted and 4 were impossible because of insufficient Pb^{2+} solubility. Specifically, a threshold $[Pb^{2+}]$ value (0.25 M) was used to eliminate reactions for which the lead cation solubilities were too low.[25] The organic ammonium iodide salts were selected to provide diversity along multiple axes, including charge, structure (linear, branched, and cyclic), and ammonium site connectivity (1, 2, and 3°). Five solvent systems (GBL, GBL/DMF, DMF, DMF/DMSO, and DMSO) were used with a single antisolvent (DCM). Note that formic acid was added to each reaction vial.

The outcomes of the 46 reactions are summarized in Figure 3. Green and blue boxes represent reactions that resulted in metal halide perovskitoids, while no solid products were observed in reactions denoted by red boxes. The white boxes represent reactions for which the threshold $[Pb^{2+}]$ could not be achieved. These reactions were not performed. Letter and number designations correspond to the specific reaction products, as listed in Table 1. Six previously reported metal halide perovskitoids and one ammonium iodide salt were observed, as marked by letter designations. Nine previously unreported metal halide perovskitoid compounds were also discovered (compounds **1**−**9**).

Replication studies between our new reaction design and more traditional designs were performed, with an 85% replication rate. All compounds denoted in Figure 3 were also synthesized under identical conditions using the traditional reactor design shown in Figure S26. Using the traditional reaction design, additional phases were occasionally observed later in the crystallization process, owing to larger amounts of the antisolvent process.

Nucleation and crystallization inherently have stochastic components. In order to estimate this effect on crystallization in the systems reported above, six identical experiments were conducted using MA and PbI_2 in GBL. Variations between experiments were minimized, so that the differences in calculated critical concentrations would be ascribed to the stochastic nature of nucleation. Plots of the calculated solvent, antisolvent, FAH, and organic and inorganic concentrations are shown in Figures S47 and S48. The magnitude of the observed variations between replicates is within the uncertainty bounds calculated by the numerical model.

Compounds **1**−**9** are constructed from similar building units. Each compound contains Pb^{2+}, octahedrally coordinated by I^- anions and protonated organic amines. The Pb−I bonds in these compounds vary in length. Pb−$I_{terminal}$ bonds range between 3.0363(6) and 3.2041(7) Å. Pb−$I_{bridging}$ interactions are generally longer, with distances between 3.1220(3) and 3.4907(6) Å. These $[PbI_6]$ coordination polyhedra remain isolated in one compound ($[dedapH]_2[PbI_6]$ (**4**)) and connect into larger molecular anions that each contain multiple $[PbI_6]$ octahedra ($[dmedH_2]_3[Pb_2I_9][CO_2H]$ (**1**), $[dmedH_2]_3[Pb_3I_{12}]\cdot 4DMF$ (**2**), and $[aepH_2]_4[Pb_3I_{12}]\text{-}[CO_2H]_2\cdot 2DMSO$ (**9**)), one-dimensional chain structures ($[dmedH_2]_2[Pb_3I_{10}]\cdot 2DMSO$ (**3**), $[dabzH_2][PbI_3]_2\cdot 2GBL\cdot 2DMF$ (**5**), $[dabzH_2][PbI_3]_2\cdot 4DMF$ (**6**), and $[dabzH_2]\text{-}[PbI_3]_2\cdot 4DMSO$ (**7**)), and a two-dimensional layer topology ($[aepH_2]_2[Pb_3I_{10}]\cdot 2DMF$ (**8**)). Polyhedral representations of the lead halide anions are shown in Figure 5.

Different anion connectivities are observed within the dimensionality classes. Three distinct molecular anions are observed in the compounds reported here. These include $[PbI_6]^{4-}$ isolated octahedra, $[Pb_2I_{6/1}I_{3/2}]^{5-}$ dimers, and

https://doi.org/10.1021/acs.chemmater.2c00247
Chem. Mater. XXXX, XXX, XXX−XXX

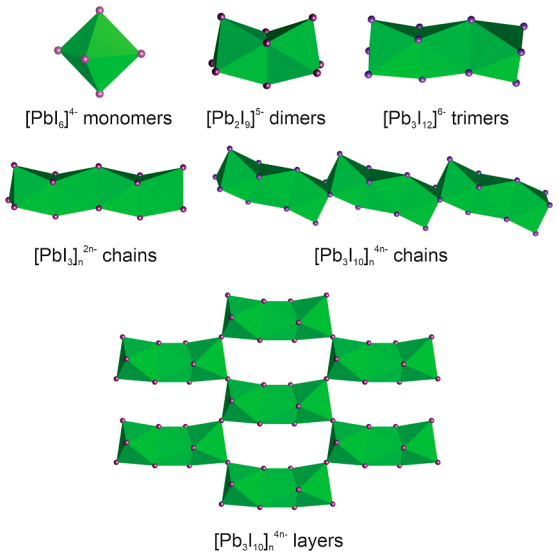

Figure 5. Polyhedral representations of the inorganic structures found in the compounds **1**−**9**. Green octahedra and purple spheres represent $[PbI_6]$ and iodine atoms, respectively.

$[Pb_3I_{6/1}I_{6/2}]^{6-}$ trimers, see Figure 5. The $[PbI_6]$ octahedra in the $[Pb_2I_{6/1}I_{3/2}]^{5-}$ dimers and $[Pb_3I_{6/1}I_{6/2}]^{6-}$ trimers are connected to one another through shared faces. Two distinct one-dimensional chains are observed, $[PbI_{6/2}]_n^{2n-}$ chains of face-shared octahedra and $[Pb_3I_{2/1}I_{4/2}I_{6/2}]_n^{4n-}$ chains. These $[Pb_3I_{2/1}I_{4/2}I_{6/2}]_n^{4n-}$ chains are essentially constructed from edge-shared $[Pb_2I_{6/1}I_{3/2}]^{5-}$ dimers, see Figure 5. The inorganic structures in compounds **1**−**9** were analyzed using bond valence sums.[36,37] Calculated ΣSi values for the Pb^{2+} cations range between 1.75 and 1.88, corresponding well with the formal charge on these metal centers. Tables showing the full bond valence sums for compounds **1**−**9** are available in the Supporting Information (Tables S3−S11).

The inorganic lead halide anions are incorporated into extended structures that include protonated organic amines and possibly formate anions and/or occluded solvent molecules. Of the nine compounds reported here, only one contains just lead iodide anions and the respective organic ammonium cation, $[dedapH]_2[PbI_6]$ (**4**). Formate anions, introduced into the reactions as formic acid, were incorporated into two compounds, $[dmedH_2]_3[Pb_2I_9][CO_2H]$ (**1**) and $[aepH_2]_4[Pb_3I_{12}][CO_2H]_2{\cdot}2DMSO$ (**9**). The remaining compounds all contain DMF ($[dmedH_2]_3[Pb_3I_{12}]{\cdot}4DMF$ (**2**), $[dabzH_2][PbI_3]_2{\cdot}4DMF$ (**6**), and $[aepH_2]_2[Pb_3I_{10}]{\cdot}2DMF$ (**8**)), DMSO ($[dmedH_2]_2[Pb_3I_{10}]{\cdot}2DMSO$ (**3**) and $[dabzH_2][PbI_3]_2{\cdot}4DMSO$ (**7**)), or both solvents ($[dabzH_2][PbI_3]_2{\cdot}2GBL{\cdot}2DMF$ (**5**)). The protonated organic amines act as hydrogen-bond donors, creating extensive hydrogen-bonding networks with the lead halide component and with GBL, DMF, DMSO, and/or formate anions. Full three-dimensional packing graphics for compounds **1**−**9** are available in the Supporting Information (Figures S27−S35).

Understanding the formation dynamics in the system described above requires more than just observational information regarding the presence or absence of crystalline products. The dynamic nature of ASVC can obscure the critical threshold parameters required to induce crystallization. As such, a one-dimensional diffusion model was used to calculate the concentrations of reactants, solvents, and antisolvents as a function of both time and position in the reaction vial, as summarized in the Experimental Section and explained in greater detail in the Supporting Information. Laser refraction was used to determine the diffusion coefficient of DCM in each solvent system.[27,28] The detailed experimentation set up for the laser refraction experiment is given in the Supporting Information. Calculated diffusion data are presented in Table 3. The rates of antisolvent evaporation and condensation were calculated using experimental meniscus height data. The rates of condensation and evaporation vary between reactions and are optimized for each experiment to match the experimental data. A consistent endpoint for the experimental modeling was also implemented based upon the addition of a fixed amount of antisolvent to the mother liquor. This cutoff value must occur

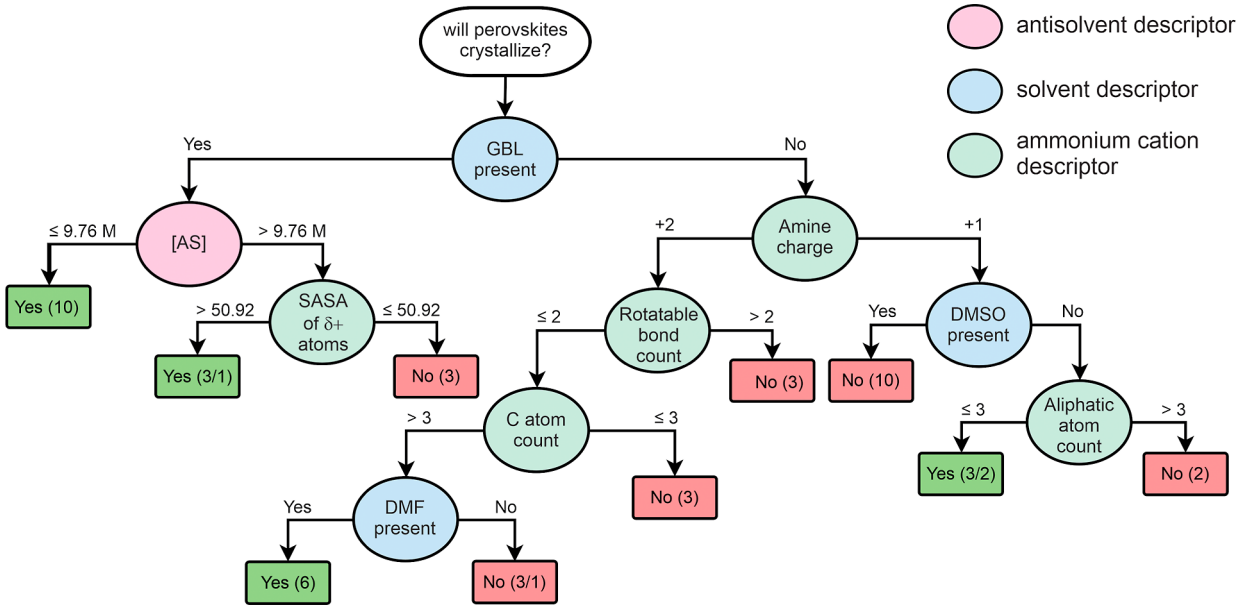

Figure 6. Metal halide perovskitoid formation decision tree. Red, blue, and green nodes represent antisolvent, solvent, and ammonium cation descriptors, respectively. Each bin contains a specific outcome value and the number of reactions correctly and incorrectly assigned to that bin.

https://doi.org/10.1021/acs.chemmater.2c00247
Chem. Mater. XXXX, XXX, XXX−XXX

before all the antisolvent evaporates from its respective vial, as the diffusion model assumes a nonzero condensation rate of the antisolvent into the mother liquor. If the modeling continues past the point of antisolvent reservoir depletion, the assumption of condensation no longer holds. The combination of experimentally determined diffusion rates in conjunction with modeled evaporation and condensation rates allows for the calculation of reactant, solvent, and antisolvent concentrations as a function of time and position, which in turn enables the elucidation of the critical concentrations of all species that are required for crystallization. A full table of these critical concentrations is available in the Supporting Information (Table S14).

An interpretable decision-tree model was used to elucidate the structure−property relationships governing crystal formation. The set of input descriptors used in this work are selected to capture "amine-", "solvent-", and "concentration"-dependent properties. Amine descriptors relevant to crystallization processes (e.g., molecular surface area, hydrogen bond donor/acceptor atom count in molecule, rotatable bond count, etc.) were computed using ChemAxon.[38] Concentration descriptors were calculated using the diffusion model. Features describing reaction conditions and inorganic and acid descriptors were excluded, as they are relatively constant across the reactions. As the goal is explanatory insights using a relatively small data set, we use an unpruned decision tree.[39] We have previously used a similar approach to gain insights into factors governing structural adaptability of amine-templated metal oxides.[40,41] Inspection of the decision tree shown in Figure 6 reveals the importance of two main aspects of crystallization in metal halide perovskitoids. First, nodes corresponding to the solvent choice indicate its importance to the reaction outcome, as shown in Figure 3. Second, amine property nodes are observed in the decision tree. Specifically, the charge of the organic ammonium cation, rotatable bond count, number of C atoms, and aliphatic atom count nodes indicate the importance of the amine structure on the reaction outcome.

Five solvent systems are used in this study, ranging from GBL to DMF and finally to DMSO. The decision tree shown in Figure 6 indicates that GBL promotes the formation of a metal halide perovskitoid, while DMSO-containing reactions are much more likely to result in no solid product. As such, GBL is a good solvent for crystallization in that the critical concentrations needed for nucleation and crystallization can be achieved through the incorporation of the antisolvent DCM. This suggests weaker GBL−reactant interactions, which contribute to lower solubilities and lower critical concentrations. DMSO, in contrast, is a poor crystallization solvent as the critical reactant concentrations are too high and cannot generally be realized during the experiments described here. This behavior mirrors critical antisolvent concentrations required to induce crystallization, shown in Figure 7. Reactions from which no metal halide perovskitoid were formed are not included in this plot.

The chemical basis for the solvent-dependent concentration trends is consistent with previous work correlating lead halide−solvent coordination strength to properties such as the Mayer Bond order[42] and Guttman donor index.[43] GBL interacts more weakly with the dissolved reactants, owing to a lower polar surface area (26.3 vs 38.8 and 36.3 for DMF and DMSO, respectively). DMF in mother liquor can form PbI_2-based Lewis adducts through dative Pb−O bonds, where the solvent acts as a Lewis base and Pb^{2+} acts as a Lewis acid.[42−45] It has been previously reported that DMF and DMSO strongly coordinate

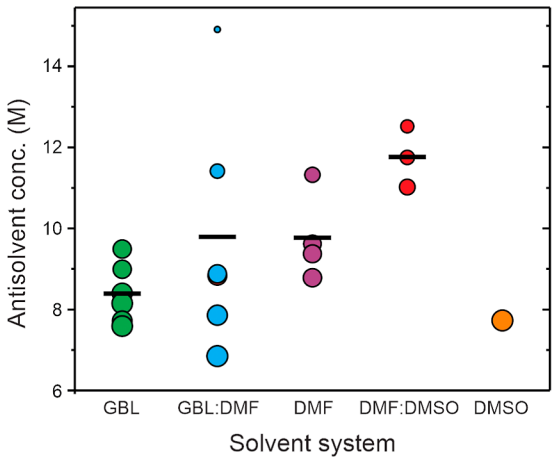

Figure 7. Critical antisolvent concentration versus solvent system plot. The circle size represents critical solvent concentration at nucleation. Black horizontal lines represent mean antisolvent concentrations within a solvent system.

with Pb^{2+} in the mother liquor and form coordination complexes, while GBL leads to the formation of clusters in the solution.[46] As the relative strength of solvent−Pb^{2+} interactions increases from GBL to DMF and DMF/DMSO, so do the relative reactant solubilities and critical concentrations required to induce crystallization. The average critical antisolvent concentrations, as a function of solvent system, shift from 8.39 to 11.76 M as one moves from GBL to DMF/DMSO.

The amine structure (indicated by green ellipses) plays an important role in the decision tree shown in Figure 6. Two main factors can be observed in the decision tree. First, increasing the strength of interaction between the organic ammonium cations and inorganic species (amine charge, SASA of $\delta+$ atoms) promotes the formation of the target compounds. Higher cation charges and greater solvent-accessible surface areas of atoms with partial positive charges both indicate stronger organic−inorganic interaction strengths, which are known to be critical in the formation of organic−inorganic hybrid materials.[42] Second, reactions involving more rigid organic cations are more likely to successfully crystallize. These descriptors (rotatable bound counts, number of carbon atoms, and aliphatic atom count) align with the well-known relationship between component rigidity (or floppiness) and crystallization.[46,47] More rigid components are much more likely to crystallize in well-ordered solids, while components with greater conformational freedom are the opposite.

In four of the reactions (1,3-dap in DMF and DMF/DMSO, aep in DMSO, and dedap in DMF) where crystal formation did not occur, liquid−liquid phase separation (LLPS) or oiling out[48,49] has been observed (shown in Figure S4a). The liquid−liquid separation results in an AS-rich phase and an AS-deficient phase. The organic ammonium cations preferentially segregate to the AS-deficient phase, hindering crystallization. This effect has been reported previously in both the halide perovskitoid[50] and organic pharmaceutical literature.[51] In our work, initial nucleation was observed to occur before liquid−liquid separation in three reactions (dmed in GBL/DMF, aep in GBL/DMF, and dedap in GBL), owing to the presence of weak GBL−reactant interactions. Images are shown in Figure S4b.

https://doi.org/10.1021/acs.chemmater.2c00247
Chem. Mater. XXXX, XXX, XXX−XXX

CONCLUSIONS

A spatiotemporal reactor design, coupled with an antisolvent diffusion model, was used to understand metal halide perovskitoid crystallization through analysis of critical species concentrations. The combination of these critical reaction parameters and the use of decision trees resulted in the elucidation of both solvent system dependencies and effects associated with the amine structure. Solvent systems that interact more weakly with dissolved lead species (GBL-containing systems) promote nucleation and crystallization, while amines that interact more strongly with inorganic components and exhibit greater rigidity are more likely to be incorporated into crystalline products. More generally, this work demonstrates that combining careful experimental design with computational data analysis can increase the insights gained from each experiment: a smaller set of experiments conducted over time can be more informative than a much larger set of parallel experiments varied in space.

ASSOCIATED CONTENT

Supporting Information

The Supporting Information is available free of charge at https://pubs.acs.org/doi/10.1021/acs.chemmater.2c00247.

Solubility measurement procedure and data; detailed reaction; image analysis description; images of all reaction outcomes; time and position data for the first observed nucleation and crystal growth; LLPS images; powder diffraction data; single-crystal synthesis details, crystal packing, layer images, and bond valence table for compounds **1**−**9**; detailed description of the refractive index measurement and diffusion model calculation; and calculated critical concentration values for all reactions along with the chemical descriptors and their descriptions. A Github repository (https://github.com/darkreactions/rapid2) contains the following files and the code/reaction block CAD file, image analysis process, and Python code for diffusion heights and crystal growth, laser diffraction for diffusion coefficient measurement and analysis, and diffusion model scripts. Supplementary crystallographic data can be obtained free of charge from The Cambridge Crystallographic Data Centre via www.ccdc.cam.ac.uk/structures (PDF).

Supplementary crystallographic data for this paper (CIF)

AUTHOR INFORMATION

Corresponding Author

Alexander J. Norquist − *Department of Chemistry, Haverford College, Haverford, Pennsylvania 19041, United States;* orcid.org/0000-0003-1040-5880; Email: anorquis@haverford.edu

Authors

Mansoor Ani Najeeb Nellikkal − *Department of Chemistry, Haverford College, Haverford, Pennsylvania 19041, United States;* orcid.org/0000-0002-8258-0613

Rodolfo Keesey − *Department of Chemistry, Haverford College, Haverford, Pennsylvania 19041, United States; Department of Chemistry, Fordham University, New York 10458, United States*

Margaret Zeile − *Department of Chemistry, Haverford College, Haverford, Pennsylvania 19041, United States*

Venkateswaran Shekar − *Department of Chemistry, Haverford College, Haverford, Pennsylvania 19041, United States*

Zhi Li − *The Molecular Foundry, Lawrence Berkeley National Laboratory, Berkeley, California 94720, United States*

Nicholas Leiby − *Two Six Technologies, Arlington, Virginia 22203, United States*

Matthias Zeller − *Department of Chemistry, Purdue University, West Lafayette, Indiana 47907, United States;* orcid.org/0000-0002-3305-852X

Emory M. Chan − *The Molecular Foundry, Lawrence Berkeley National Laboratory, Berkeley, California 94720, United States;* orcid.org/0000-0002-5655-0146

Joshua Schrier − *Department of Chemistry, Fordham University, New York 10458, United States;* orcid.org/0000-0002-2071-1657

Complete contact information is available at: https://pubs.acs.org/10.1021/acs.chemmater.2c00247

Author Contributions

M.A.N., J.S., and A.J.N. conceived the project. M.A.N., M.Z., and Z.L. performed synthesis, characterization, and data analysis of reaction products. R.K. performed the diffusion modeling. N.L. and V.S. participated in software development. M.Z. collected and refined single-crystal X-ray diffraction data. E.M.C., J.S., and A.J.N. supervised the project. All authors contributed to the preparation of the manuscript.

Notes

The authors declare no competing financial interest.

ACKNOWLEDGMENTS

This study is based upon work supported by the Defense Advanced Research Projects Agency (DARPA) under contract no. HR001118C0036. Any opinions, findings, and conclusions or recommendations expressed in this material are those of the authors and do not necessarily reflect the views of DARPA. M.A.N. acknowledges the Solmssen's for their support. Work at the Molecular Foundry was supported by the Office of Science, Office of Basic Energy Sciences, of the U.S. Department of Energy under contract no. DE-AC02-05CH11231. J.S. acknowledges the Henry Dreyfus Teacher-Scholar Award (TH-14-010) and resources of the MERCURY consortium (http://mercuryconsortium.org/) under NSF grants CNS-2018427. M.Z. acknowledges the National Science Foundation, Major Research Instrumentation Program under grant no. CHE 1625543, for funding for the single-crystal X-ray diffractometer.

REFERENCES

(1) Leijtens, T.; Eperon, G. E.; Noel, N. K.; Habisreutinger, S. N.; Petrozza, A.; Snaith, H. J. Stability of metal halide perovskite solar cells. *Adv. Energy Mater.* **2015**, *5*, 1500963.

(2) Qiu, L.; He, S.; Ono, L. K.; Liu, S.; Qi, Y. Scalable fabrication of metal halide perovskite solar cells and modules. *ACS Energy Lett.* **2019**, *4*, 2147−2167.

(3) Wang, S.; Li, X.; Wu, J.; Wen, W.; Qi, Y. Fabrication of efficient metal halide perovskite solar cells by vacuum thermal evaporation: A progress review. *Curr. Opin. Electrochem.* **2018**, *11*, 130−140.

(4) Niu, T.; Xue, Q.; Yip, H.-L. Molecularly Engineered Interfaces in Metal Halide Perovskite Solar Cells. *J. Phys. Chem. Lett.* **2021**, *12*, 4882−4901.

(5) Lim, K.-G.; Han, T.-H.; Lee, T.-W. Engineering electrodes and metal halide perovskite materials for flexible/stretchable perovskite solar cells and light-emitting diodes. *Energy Environ. Sci.* **2021**, *14*, 2009−2035.

(6) Bao, C.; Yang, J.; Bai, S.; Xu, W.; Yan, Z.; Xu, Q.; Liu, J.; Zhang, W.; Gao, F. High performance and stable all-inorganic metal halide perovskite-based photodetectors for optical communication applications. *Adv. Mater.* **2018**, *30*, 1803422.
(7) Wang, H. P.; Li, S.; Liu, X.; Shi, Z.; Fang, X.; He, J. H. Low-Dimensional Metal Halide Perovskite Photodetectors. *Adv. Mater.* **2021**, *33*, 2003309.
(8) Feng, J.; Gong, C.; Gao, H.; Wen, W.; Gong, Y.; Jiang, X.; Zhang, B.; Wu, Y.; Wu, Y.; Fu, H.; Jiang, L.; Zhang, X. Single-crystalline layered metal-halide perovskite nanowires for ultrasensitive photodetectors. *Nat. Electron.* **2018**, *1*, 404−410.
(9) Hao, D.; Zou, J.; Huang, J. Recent developments in flexible photodetectors based on metal halide perovskite. *InfoMat* **2020**, *2*, 139−169.
(10) Hu, Z.; Liu, Z.; Zhan, Z.; Shi, T.; Du, J.; Tang, X.; Leng, Y. Advances in metal halide perovskite lasers: synthetic strategies, morphology control, and lasing emission. *Adv. Photonics* **2021**, *3*, 034002.
(11) Zhang, Q.; Shang, Q.; Su, R.; Do, T. T. H.; Xiong, Q. Halide perovskite semiconductor lasers: materials, cavity design, and low threshold. *Nano Lett.* **2021**, *21*, 1903−1914.
(12) Lei, L.; Dong, Q.; Gundogdu, K.; So, F. Metal Halide Perovskites for Laser Applications. *Adv. Funct. Mater.* **2021**, *31*, 2010144.
(13) Ye, T.; Fu, W.; Wu, J.; Yu, Z.; Jin, X.; Chen, H.; Li, H. Single-crystalline lead halide perovskite arrays for solar cells. *J. Mater. Chem. A* **2016**, *4*, 1214−1217.
(14) Zhang, T.; Yang, M.; Benson, E. E.; Li, Z.; van de Lagemaat, J.; Luther, J. M.; Yan, Y.; Zhu, K.; Zhao, Y. A facile solvothermal growth of single crystal mixed halide perovskite $CH_3NH_3Pb(Br_{1-x}Cl_x)_3$. *Chem. Commun.* **2015**, *51*, 7820−7823.
(15) Saidaminov, M. I.; Abdelhady, A. L.; Murali, B.; Alarousu, E.; Burlakov, V. M.; Peng, W.; Dursun, I.; Wang, L.; He, Y.; Maculan, G. High-quality bulk hybrid perovskite single crystals within minutes by inverse temperature crystallization. *Nat. Commun.* **2015**, *6*, 1−6.
(16) Liu, Y.; Yang, Z.; Cui, D.; Ren, X.; Sun, J.; Liu, X.; Zhang, J.; Wei, Q.; Fan, H.; Yu, F.; Zhang, X.; Zhao, C.; Liu, S. F. Two-Inch-Sized Perovskite $CH_3NH_3PbX_3$ (X = Cl, Br, I) Crystals: Growth and Characterization. *Adv. Mater.* **2015**, *27*, 5176−5183.
(17) Dong, Q.; Fang, Y.; Shao, Y.; Mulligan, P.; Qiu, J.; Cao, L.; Huang, J. Solar cells. Electron-hole diffusion lengths > 175 μm in solution-grown $CH_3NH_3PbI_3$ single crystals. *Science* **2015**, *347*, 967−970.
(18) Shi, D.; Adinolfi, V.; Comin, R.; Yuan, M.; Alarousu, E.; Buin, A.; Chen, Y.; Hoogland, S.; Rothenberger, A.; Katsiev, K.; Losovyj, Y.; Zhang, X.; Dowben, P. A.; Mohammed, O. F.; Sargent, E. H.; Bakr, O. M. Low trap-state density and long carrier diffusion in organolead trihalide perovskite single crystals. *Science* **2015**, *347*, 519−522.
(19) Yang, Y.; Yan, Y.; Yang, M.; Choi, S.; Zhu, K.; Luther, J. M.; Beard, M. C. Low surface recombination velocity in solution-grown $CH_3NH_3PbBr_3$ perovskite single crystal. *Nat. Commun.* **2015**, *6*, 7961.
(20) Zuo, C.; Ding, L. Lead-free Perovskite Materials $(NH_4)_3Sb_2I_xBr_{9-x}$. *Angew. Chem.* **2017**, *129*, 6628−6632.
(21) Wei, H.; Fang, Y.; Mulligan, P.; Chuirazzi, W.; Fang, H.-H.; Wang, C.; Ecker, B. R.; Gao, Y.; Loi, M. A.; Cao, L.; Huang, J. Sensitive X-ray detectors made of methylammonium lead tribromide perovskite single crystals. *Nat. Photonics* **2016**, *10*, 333−339.
(22) Udayabhaskararao, T.; Kazes, M.; Houben, L.; Lin, H.; Oron, D. Nucleation, growth, and structural transformations of perovskite nanocrystals. *Chem. Mater.* **2017**, *29*, 1302−1308.
(23) Kirman, J.; Johnston, A.; Kuntz, D. A.; Askerka, M.; Gao, Y.; Todorović, P.; Ma, D.; Privé, G. G.; Sargent, E. H. Machine-learning-accelerated perovskite crystallization. *Matter* **2020**, *2*, 938−947.
(24) Li, Z.; Nega, P. W.; Nellikkal, M. A. N.; Dun, C.; Zeller, M.; Urban, J. J.; Saidi, W. A.; Schrier, J.; Norquist, A. J.; Chan, E. M. Dimensional control over metal halide perovskite crystallization guided by active learning. *Chem. Mater.* **2022**, *34*, 756−767.
(25) Li, Z.; Najeeb, M. A.; Alves, L.; Sherman, A. Z.; Shekar, V.; Cruz Parrilla, P.; Pendleton, I. M.; Wang, W.; Nega, P. W.; Zeller, M.; Schrier, J.; Norquist, A. J.; Chan, E. M. Robot-accelerated perovskite investigation and discovery. *Chem. Mater.* **2020**, *32*, 5650−5663.
(26) Fick, A. Ueber Diffusion. *Ann. Phys.* **1855**, *170*, 59−86.
(27) Coutinho, C. A.; Mankidy, B. D.; Gupta, V. K. A Simple Refraction Experiment for Probing Diffusion in Ternary Mixtures. *Chem. Eng. Educ.* **2010**, *44*, 134−139.
(28) Dok-Yong, J.; Jong-Hyon, J.; Nam-Chol, K. A Measurement Method of Diffusion Coefficient of Liquid Using Radial Laser Rays Formed By Cylindrical Refractive System Submission date 29, Aug. **2017**, arXiv>physics>Instrumentation and Detectors. arXiv:1709.01595.
(29) Kim, J. S.; Wu, Z.; Morrow, A. R.; Yethiraj, A.; Yethiraj, A. Self-Diffusion and Viscosity in Electrolyte Solutions. *J. Phys. Chem. B* **2012**, *116*, 12007−12013.
(30) Nelder, J. A.; Mead, R. A Simplex Method for Function Minimization. *Comput. J.* **1965**, *7*, 308−313.
(31) Pendleton, I. M.; Cattabriga, G.; Li, Z.; Najeeb, M. A.; Friedler, S. A.; Norquist, A. J.; Chan, E. M.; Schrier, J. Experiment Specification, Capture and Laboratory Automation Technology (ESCALATE): a software pipeline for automated chemical experimentation and data management. *MRS Commun.* **2019**, *9*, 846−859.
(32) Glor, E. C.; Blau, S. M.; Yeon, J.; Zeller, M.; Shiv Halasyamani, P.; Schrier, J.; Norquist, A. J. $[R\text{-}C_7H_{16}N_2][V_2Te_2O_{10}]$ and $[S\text{-}C_7H_{16}N_2][V_2Te_2O_{10}]$; new polar templated vanadium tellurite enantiomers. *J. Solid State Chem.* **2011**, *184*, 1445−1450.
(33) Holmes, G.; Donkin, A.; Witten, I. H. WEKA: a machine learning workbench. *Proceedings of ANZIIS '94 - Australian New Zealnd Intelligent Information Systems Conference, 29 Nov−2 Dec. 1994*, 1994, pp 357−361.confproc
(34) Hssina, B.; Merbouha, A.; Ezzikouri, H.; Erritali, M. A comparative study of decision tree ID3 and C4.5. *Int. J. Adv. Comput. Sci. Appl.* **2014**, *4*, 13−19.
(35) Bindhia, K. F.; Vijayalakshmi, Y.; Manimegalai, P.; Babu, S. S. Classification Using Decision Tree Approach towards Information Retrieval Keywords Techniques and a Data Mining Implementation Using WEKA Data Set. *Int. J. Pure Appl. Math.* **2017**, *116*, 19−29.
(36) Brown, I. D.; Altermatt, D. Bond-valence parameters obtained from a systematic analysis of the inorganic crystal structure database. *Acta Crystallogr., Sect. B: Struct. Sci.* **1985**, *41*, 244−247.
(37) Guo, Y.-Y.; Yang, L.-J.; Lightfoot, P. Three new lead iodide chain compounds, APbI3, templated by molecular cations. *Crystals* **2019**, *9*, 616.
(38) ChemAxon Marvin Version 21.4.0. https://chemaxon.com/ (accessed October 04, 2021).
(39) Esposito, F.; Malerba, D.; Semeraro, G.; Kay, J. A comparative analysis of methods for pruning decision trees. *IEEE Trans. Pattern Anal. Mach. Intell.* **1997**, *19*, 476−493.
(40) Adler, P. D. F.; Xu, R.; Olshansky, J. H.; Smith, M. D.; Elbert, K. C.; Yang, Y.; Ferrence, G. M.; Zeller, M.; Schrier, J.; Norquist, A. J. Probing structural adaptability in templated vanadium selenites. *Polyhedron* **2016**, *114*, 184−193.
(41) Raccuglia, P.; Elbert, K. C.; Adler, P. D. F.; Falk, C.; Wenny, M. B.; Mollo, A.; Zeller, M.; Friedler, S. A.; Schrier, J.; Norquist, A. J. Machine-learning-assisted materials discovery using failed experiments. *Nature* **2016**, *533*, 73−76.
(42) Stevenson, J.; Sorenson, B.; Subramaniam, V. H.; Raiford, J.; Khlyabich, P. P.; Loo, Y.-L.; Clancy, P. Mayer bond order as a metric of complexation effectiveness in lead halide perovskite solutions. *Chem. Mater.* **2017**, *29*, 2435−2444.
(43) Hamill, J. C., Jr.; Schwartz, J.; Loo, Y.-L. Influence of Solvent Coordination on Hybrid Organic-Inorganic Perovskite Formation. *ACS Energy Lett.* **2017**, *3*, 92−97.
(44) Wharf, I.; Gramstad, T.; Makhija, R.; Onyszchuk, M. Synthesis and vibrational spectra of some lead(II) halide adducts with O-, S-, and N-donor atom ligands. *Can. J. Chem.* **1976**, *54*, 3430−3438.
(45) Cao, X.; Zhi, L.; Li, Y.; Fang, F.; Cui, X.; Yao, Y.; Ci, L.; Ding, K.; Wei, J. Elucidating the key role of a Lewis base solvent in the formation of perovskite films fabricated from the Lewis adduct approach. *ACS Appl. Mater. Interfaces* **2017**, *9*, 32868−32875.

https://doi.org/10.1021/acs.chemmater.2c00247
Chem. Mater. XXXX, XXX, XXX−XXX

(46) Fateev, S. A.; Petrov, A. A.; Khrustalev, V. N.; Dorovatovskii, P. V.; Zubavichus, Y. V.; Goodilin, E. A.; Tarasov, A. B. Solution processing of methylammonium lead iodide perovskite from γ-butyrolactone: crystallization mediated by solvation equilibrium. *Chem. Mater.* **2018**, *30*, 5237−5244.
(47) Wicker, J. G. P.; Cooper, R. I. Beyond rotatable bond counts: capturing 3D conformational flexibility in a single descriptor. *J. Chem. Inf. Model.* **2016**, *56*, 2347−2352.
(48) Deneau, E.; Steele, G. An in-line study of oiling out and crystallization. *Org. Process Res. Dev.* **2005**, *9*, 943−950.
(49) Meng, Z.; Huang, Y.; Cheng, S.; Wang, J. Investigation of Oiling-Out Phenomenon of Small Organic Molecules in Crystallization Processes: A Review. *ChemistrySelect* **2020**, *5*, 7855−7866.
(50) Zhang, Y.; Siegler, T. D.; Thomas, C. J.; Abney, M. K.; Shah, T.; De Gorostiza, A.; Greene, R. M.; Korgel, B. A. A "tips and tricks" practical guide to the synthesis of metal halide perovskite nanocrystals. *Chem. Mater.* **2020**, *32*, 5410−5423.
(51) Li, X.; Yin, Q.; Zhang, M.; Hou, B.; Bao, Y.; Gong, J.; Hao, H.; Wang, Y.; Wang, J.; Wang, Z. Antisolvent crystallization of erythromycin ethylsuccinate in the presence of liquid−liquid phase separation. *Ind. Eng. Chem. Res.* **2016**, *55*, 766−776.
(52) Xie, J.; Liu, Y.; Liu, J.; Lei, L.; Gao, Q.; Li, J.; Yang, S. Study on the correlations between the structure and photoelectric properties of $CH_3NH_3PbI_3$ perovskite light-harvesting material. *J. Power Sources* **2015**, *285*, 349−353.
(53) Umeyama, D.; Lin, Y.; Karunadasa, H. I. Red-to-Black Piezochromism in a Compressible Pb-I-SCN Layered Perovskite. *Chem. Mater.* **2016**, *28*, 3241−3244.
(54) Im, J.-H.; Chung, J.; Kim, S.-J.; Park, N.-G. Synthesis, structure, and photovoltaic property of a nanocrystalline 2H perovskite-type novel sensitizer $(CH_3CH_2NH_3)PbI_3$. *Nanoscale Res. Lett.* **2012**, *7*, 1−7.
(55) Dou, S.-q.; Paulus, H.; Weiss, A. Crystal structure and halogen NQR of diammoniumalkane halides. *J. Mol. Struct.* **1995**, *345*, 1−10.
(56) Calabrese, J.; Jones, N. L.; Harlow, R. L.; Herron, N.; Thorn, D. L.; Wang, Y. Preparation and characterization of layered lead halide compounds. *J. Am. Chem. Soc.* **1991**, *113*, 2328−2330.

https://doi.org/10.1021/acs.chemmater.2c00247
Chem. Mater. XXXX, XXX, XXX−XXX